3D microprinting of inorganic porous materials by chemical linking-induced solidification of nanocrystals

Minju Song
Ulsan National Institute of Science and Technology (UNIST)
Yoonkyum Kim
Ulsan National Institute of Science and Technology (UNIST)
Du San Baek
https://orcid.org/0000-0003-0446-5668
Da Hwi Gu
Ulsan National Institute of Science and Technology
Benjamin Cunning
Ulsan National Institute of Science and Technology (UNIST)
Seong Eun Yang
Ulsan National Institute of Science and Technology
Seung Hwae Heo
Ulsan National Institute of Science and Technology
Seunghyun Lee
Ulsan National Institute of Science and Technology (UNIST)
Jung-Woo Yoo
Ulsan National Institute of Science and Technology https://orcid.org/0000-0001-7038-4001
Sang Hoon Joo
Ulsan National Institute of Science and Technology https://orcid.org/0000-0002-8941-9662
Rodney Ruoff
Center for Multidimensional Carbon Materials (CMCM), Institute for Basic Science (IBS)
https://orcid.org/0000-0002-6599-6764
Jae Sung Son (jsson@unist.ac.kr)
Ulsan National Institute of Science and Technology (UNIST) https://orcid.org/0000-0003-3498-9761

Article

Keywords:

Posted Date: February 15th, 2023

DOI: https://doi.org/10.21203/rs.3.rs-2580380/v1

Abstract

Three-dimensional (3D) microprinting is considered a next-generation manufacturing process for the production of microscale components; however, the narrow range of suitable materials, which include mainly polymers, is a critical issue that limits the application of this process to functional inorganic materials. Herein, we develop a generalised microscale 3D printing method for the production of purely inorganic nanocrystal-based porous materials. Our process was designed to solidify all-inorganic nanocrystals via immediate dispersibility control and surface linking in the nonsolvent linker bath and thereby created multibranched gel networks. The process works with various inorganic materials, including metals, semiconductors, magnets, oxides, and multi-materials, not requiring organic binders or stereolithographic equipment. Filaments with a diameter of sub-10 μm are printed into designed complex 3D microarchitectures, which exhibit full nanocrystal functionality and high specific surface areas comparable to those of typical aerogels. This approach enables the manufacture of a very broad range of functional inorganic materials.

Main

Additive manufacturing, commonly known as 3D printing technology, allows the production of materials with customised shapes and dimensions[1,2]. In particular, micro-stereolithography techniques[3,4] and direct ink writing[5] can revolutionise the manufacturing of microscale components for various applications, including micromechanics, microelectronics, and biomedical systems by enabling the creation of previously inaccessible 3D architectures[6–10]. Micro-stereolithography is based on multiphoton absorption and is achieved using a projection lens, while direct ink writing employs microneedles; however, these processes critically rely on organic or polymer-based resin inks to ensure photocurability or rheological printability in the optical lithography or ink writing process, respectively, which limit the range of printable materials and the intrinsic functionality of the printed objects. Nanomaterial-based polymer resin-free printing techniques were recently developed by introducing photocurable molecules to the nanomaterial surfaces[11,12]. Sun et al. achieved the stereolithographic 3D nanoprinting of quantum dots by exploiting photoexcitation-driven chemical bonding[12]. Despite these recent successes, existing processes for inorganic nanomaterials or composites are only applicable to specific photo-active materials and require special lithographic equipment. Thus, new processes are required to diversify and expand the range of inorganic materials suitable for 3D microprinting.

Colloidal nanocrystals have emerged as versatile inorganic building blocks of functional 2D and 3D solids with tailorable physicochemical properties[13–15], while advances in synthetic methodology have enabled the preparation of colloidal particles of almost any inorganic functional material[16–18]. In particular, the assembly of colloidal nanocrystals into macroscopic solid gels introduces a new class of inorganic porous material with high surface areas and low densities, whose electronic, magnetic, and optical properties originate from building blocks[19–21], and can thus be tailored to a wide variety of applications, including energy storage and conversion[22,23], catalysis[24,25], adsorbent[26], filter[27], and

electrodes[28], and sensors[29]. Herein, we demonstrate a generalised method to achieve high-resolution wet 3D microprinting of inorganic porous materials by the direct writing of purely inorganic colloidal nanocrystal ink in the linker-containing nonsolvent bath (Fig. 1a). This process is applicable to a diverse range of materials and produces crystalline nanostructures with high structural integrity. Further, the process is tailored toward the creation of purely inorganic materials with 3D microarchitectures and does not require any polymer resins. The inorganic ligand-capped nanocrystal inks were solidified by the instant interconnection of the nanocrystals through solvent polarity change and surface linking during the ink extrusion, which affords a multibranched gel network (Fig. 1b). The dimension-controlled printing of microscale filaments creates complex 3D architectures, which retain the functionalities of the primary nanocrystals and exhibit high specific surface areas comparable to those of existing nanocrystal-based and sol-gel-processed aerogels. Further, our method produced multiple materials using mixed nanocrystal inks or sequential printing.

Wet 3d Microprinting Of Inorganic Nanocrystals

The developed wet 3D microprinting method involves three steps: i) preparation of a negatively charged nanocrystal inks, ii) controlled solidification of the extruded nanocrystals in the nonsolvent bath containing linker ions, and iii) supercritical drying of the wet-state of printed objects into the solid-state 3D architectures. Inorganic ligand (*i.e.*, tetrathiomolybdate; MoS_4^{2-})-capped nanocrystals dispersed in polar solvent (*i.e.*, N-methylformamide (NMF)) were exploited as printing inks, which are extruded into nonsolvent with lower dielectric constant (*i.e.*, butanol) containing linker ions. Instantaneous solvent-to-nonsolvent mixing during the ink extrusion instantly reduces the diserpsiblity of negatively charged nanocrystals, resulting in agglomeration of nanocrystals. Systematic studies on the combination of solvent (NMF) and nonsolvent with respect to their solubility parameters and dielectric constants reveal that the optimum ranges are essential to flocculate nanocrystals (Supplementary Fig. 1 and Supplementary Table 1). When the differences in solubility parameters of nonsolvent with NMF exceeded certain limits, their phases are separated. Also, the nonsolvent with high dielectric constant solubilized the negatively charged nanocrystals. Under the optimum ranges of both characteristics of nonsolvent, the instant agglomeration of nanocrystals was achieved (Supplementary Fig. 2, 3 and Supplementary Table 1).

Multivalent metal ion linkers play the role of creating covalent bonds with the surface inorganic ligands among nanocrystals in agglomerates which enhance the overall structural entanglement (Supplementary Fig. 4), eventually leading to the robust solidification. Since the thiomolybdate anion ligand (*i.e.*, a soft Lewis base) has chemical affinity to metal ion linkers that act as soft Lewis acids[30,31], soft Lewis acids of multivalent coordinating ions, including Au^{3+}, Pt^{4+}, and Fe^{2+} but not limited, were chosen to serve as metal linkers (e.g. Au^{3+} linker for Au and Ag nanocrystals, Pt^{4+} for FePt nanocrystals, and Fe^{2+} for CdSe and Fe_3O_4 nanocrystals). The linking of the nanocrystals was optimised using the control parameters of the concentrations of both the metal ion linkers and the nanocrystals. When the concentrations of either the nanocrystals or the coordinating linker ions exceeded certain limits, the nozzle was easily clogged,

causing discontinuous ink deposition (Supplementary Fig. 5). In contrast, decreasing their concentrations “too far” caused the dissolution of nanocrystals into the linker bath, and we could not obtain the defined filaments by printing (Supplementary Fig. 5). In turn, under optimum conditions, defined 3D inorganic filaments with multibranched porous nanocrystal networks were printed by our process.

A model system consisting of thiomolybdate-capped Ag nanocrystal building blocks was studied. The electrokinetic ξ-potentials changed from − 50.7 to − 10.1 mV during the deposition, indicating that the nanocrystals lost their surface charges upon coordination of the metal ion linkers (Supplementary Fig. 6). Moreover, the peaks in the S 2p region of the X-ray photoelectron spectroscopy (XPS) spectrum showed a peak shift to higher binding energies upon ligation to metal ions, while the Ag 3d peaks did not change (Supplementary Fig. 7). This result confirms that no reaction occurred between the metal ions and the nanocrystals occurs, but rather, the nanocrystals were bridged by linking the surface thiometallate ligands with metal ions.

The system used to print the inorganic nanocrystals consisted of a micropipette nozzle connected to a syringe-type reservoir containing negatively charged inorganic nanocrystals, which were extruded using a pneumatic pressure controller. The stage mounted with the linker-containing solidification bath was moved along the *x*-, *y*-, and *z*-axes in a pre-designed model (Supplementary Fig. 8). The diameters of the filaments were precisely controlled from 8 to 49 μm in the wet state by adjusting the nozzle diameter; thus, the method demonstrates microscale printability. The wet filaments were further dried by supercritical CO_2 drying, effectively generating extremely microporous materials without substantial structural shrinkage or distortion, as shown in the optical microscopy (OM) images (Fig. 1c, d). Scanning electron microscopy (SEM) images (Fig. 1f–i) confirmed that the dried filaments constructed from Ag nanocrystals showed uniform linewidths with controllable diameters ranging from 7 to 44 μm (Fig. 1e). High-resolution (HR) SEM images clearly revealed extremely porous and multibranched networks in all samples, which showed characteristics of typical aerogels (Fig. 1f–i, insets).

This ability to print microscale inorganic filaments enables the construction of complex 3D architectures in diverse ranges of materials. For example, a 3D cubic lattice structure was built via the layer-by-layer deposition of 32 Ag filament layers in a single pass (Fig. 2a, Supplementary Fig. 9, Supplementary Video 1). The printing method showed high precision, while the printed 3D architectures exhibited excellent structural fidelity and were consistent with the design model (Fig. 2a, inset). The 3D-printed filaments maintained a circular cross section with a uniform diameter (Fig. 2b, c, Supplementary Fig. 9). Energy dispersive X-ray spectroscopy (EDS) maps showed that Ag nanocrystals, S-based ligands, and Au-based linkers were confined to the patterned layers (Fig. 2d). Lattice structures were printed using various materials, including metallic Au, magnetic FePt and Fe_3O_4, and semiconducting CdSe nanocrystals (Fig. 2e–h). SEM images and EDS maps confirm that all samples show high structural and compositional integrity and uniformity (Supplementary Fig. 10). Various 3D objects were printed, including a CdSe-based pyramid (Fig. 2i, Supplementary Video 2) and a FePt-based hexagonal prism (Fig. 2j, Supplementary Video 3), which all showed excellent lateral and vertical shape fidelity. Moreover, a large square lattice pattern with dimensions of 1.2 mm $\times$ 1.2 mm was constructed by the layer-by-layer

printing of 8 Ag filament layers (Fig. 2k), thereby demonstrating the feasibility of the printing process over a millimetre-scale area. These examples of complex 3D architectures built from various nanocrystals clearly demonstrate the microscale 3D printability of the method and the wide range of applicable materials.

Microstructural Characteristics

Low-resolution and HRSEM images of the printed structures reveal porous microstructures with interconnected networks of extremely thin wire-like structures with numerous bifurcations (Fig. 3a, b). The typical dimensions of these multibranched wire-like structures are on the same size scale as the diameter of the original nanocrystals (5–10 nm), which demonstrates that the printed structures were formed directly from the original colloidal nanocrystal building blocks without the formation of any kind of secondary structures. A diverse range of pore sizes was observed, ranging from a few nanometres to several hundreds of nanometres. TEM images (Fig. 3c, Supplementary Fig. 11) show that the nanocrystals were not merged, but rather maintained their primary shapes and sizes, which supports the hypothesis that the solidification of nanocrystals is induced by the surface linking reaction. The random orientation of the nanocrystals in the chains, as seen in the HRTEM images, resulted in ring-like electron diffraction patterns (Fig. 3d). X-ray diffraction (XRD) spectra of the as-synthesized nanocrystals and printed structures were essentially identical in terms of the observed peak widths and positions (Fig. 3e, Supplementary Fig. 12), further suggesting the prefect or near-perfect persistence of the nanocrystals through the entire process. Thermogravimetric analysis of the 3D-printed Au showed total weight losses of less than 5%, even at temperatures as high as 700°C (Supplementary Fig. 13), considerably lower than the 20 ~ 30% weight loss typically observed in organic-capped nanocrystal-based aerogels. This result further illustrates the stability of the printed inorganic aerogels.

The specific surface area and porosity of the printed structures were evaluated using nitrogen adsorption/desorption isotherms. All samples exhibited typical type II isotherms with type H3 hysteresis loops similar to those of known nanocrystal-based aerogels at high relative pressures (Fig. 3f, Supplementary Fig. 14). The pore size distribution plots of the printed structures confirm the broad pore size distribution (almost independent of the materials), indicating that the formation of pores was induced by the surface bridging of nanocrystals and was therefore independent of the characteristics of the nanocrystal cores (Fig. 3f inset, Supplementary Fig. 15). The printed Fe_3O_4 and Au samples showed the highest (279 $m^2\ g^{-1}$) and lowest (54.2 $m^2\ g^{-1}$) Brunauer-Emmett-Teller (BET) surface areas, respectively, which is in good agreement with those of reported nanocrystal-based aerogels. The mole-based surface areas of the printed materials are very high because the molecular weights of these materials are significantly higher than those of well-known silica aerogels. The silica-equivalent surface areas of the 3D-printed structures ranged from ~ 300 to ~ 600 $m^2\ g^{-1}$ (Fig. 3g, Supplementary Table 2), which are comparable to those of nanocrystal- and oxide-based aerogels[32–39].

Diverse Functionality Of Printed Materials

The solidification of the inorganic nanocrystals induced by the surface-linking reaction effectively conserved the primary functionalities of the nanocrystals in the 3D-printed structures. For example, the 3D-printed Fe_3O_4 exhibited superparamagnetic properties like those of the as-synthesised Fe_3O_4 nanocrystals, with a blocking temperature of 28 K, and in good agreement with the preserved nano-structural characteristics observed in the SEM and TEM images (Supplementary Fig. 15). The magnetization curves also confirm the conservation of the magnetic properties of Fe_3O_4 nanocrystals, showing that the saturation magnetization and coercive fields of printed and as-synthesized nanocrystals at 2 K and 300 K were essentially identical (Fig. 3h). As another example, the 3D-printed wet and dried CdSe structures retained the excitonic features of the CdSe semiconductor nanocrystals. Even though a small red-shift and peak broadening were observed in the absorption spectrum owing to electronic coupling among nanocrystals in the connected networks, the printed CdSe still exhibit a relatively sharp onset, indicating that the quantum confinement effect of the nanocrystals is retained in the printed structure (Supplementary Fig. 16). The luminescent properties of the printed CdSe were recovered by the photooxidation treatment, although the luminescent properties of the inorganic CdSe nanocrystals in the ink were initially quenched via the surface exchange with the inorganic thiometallate ligands, which introduced numerous surface traps that cause non-radiative recombination. Our previous work described that the photooxidation of inorganic ligand-capped CdSe nanocrystals enhances their luminescent properties by the passivation of surface dangling bonds via surface oxidation[40]. The printed CdSe exhibits relatively sharp emission along with a small blue-shift and peak broadening in the photoluminescent (PL) spectrum (Fig. 3i). This is coincident with the absorption spectrum, which shows the peak shift and broadening, indicating that the PL properties originate from the band edges rather than the surface trap states. The blue shifts observed in the CdSe solid were attributed to deep surface oxidation, which reduced the size of the CdSe core. As a third example, the electronic coupling between metal nanocrystals in the percolating porous structure was responsible for its favourable electrical transport properties (Fig. 3j, Supplementary Fig. 17). The 3D-printed and CO_2-dried Au sample exhibited an electrical conductivity of 4.0×10^1 S m^{-1}, which is within in the reported range of the reported conductivities of porous metal materials[41]. Drying the wet Au sample under ambient conditions induced a transformation into a denser xerogel with a significantly enhanced electrical conductivity of 1.9×10^3 S m^{-1}. Heat treatment at 600°C further increased the electrical conductivity to 1.4×10^6 S m^{-1}, which is within the range of the conductivities of micro-patterned electrodes in microelectronic systems[42].

3d Printing Of Multi-material Architectures

Porous structures with multiple material compositions were 3D-printed by sequentially printing different nanocrystal inks, or by printing mixed inks containing different nanocrystals. A combination of Au and CdSe nanocrystals was selected as a model system because metal-semiconductor hybrid systems have broad applications in photonics, optoelectronics, and photocatalysis[43]. A lattice structure with alternating

Au and CdSe layers was obtained via the sequential printing of Au and CdSe nanocrystal inks (Fig. 4a). SEM and EDS images showed good separation between the vertical Au and horizontal CdSe layers, without merging at the junctions (Fig. 4b–d). The printed lattice of the mixed Au-CdSe yielded a homogeneous composition of Au and CdSe phases, as confirmed by SEM and EDS images (Fig. 4e–h). The microstructural morphology of the highly porous network was similar to that of single nanocrystal-based samples (Fig. 4f inset). The STEM-EDS maps and high angle annular dark field-scanning TEM (HAADF-STEM) images showed that the Au and CdSe nanocrystals were isolated in the porous multibranched network (Fig. 4i). The absorption spectrum and XRD pattern confirmed that the Au and CdSe nanocrystals were retained in the composite structure, without atomic-scale structural rearrangements or changes in the electronic spectra (Fig. 4j, k). The BET surface area (132 $m^2 g^{-1}$) was similar to the average value of the Au and CdSe printed structures, reflecting its homogeneity (Fig. 4l). These results demonstrate the straightforward 3D printing of multiple materials with multifunctional and synergistic features using our method.

Conclusion

We report the development of a high-precision 3D printing method for the production of sub-10 μm inorganic porous architectures by the ink writing of inorganic nanocrystals in a linker-containing nonsolvent bath. Controlling dispersibility and the subsequent surface linking reaction of the nanocrystals enabled their instant connection during the ink extrusion to produce high-fidelity 3D microarchitectures. This chemical strategy enables the 3D microprinting of a diverse range of functional materials, including metals, semiconductors, magnets, oxides, and so-called “multi-materials”, without the use of organic binders or special lithographic equipment. By incorporating low-dimensional materials, such as 1D and 2D materials and molecular clusters, we are confident that our process can be extended for printing an even broader range of inorganic materials with 3D micro-architectures and diverse functionalities. This approach conserves the microstructural porosity and properties of the building blocks in the 3D-printed inorganic structures, and will, we suggest, enable their wider implementation in thermal, catalytic, electronic, optical, and magnetic components, and in the manufacture of micro-inorganics for microelectronics, micromechanics, and biomedical systems.

References

1. Truby RL, Lewis JA (2016) Printing soft matter in three dimensions. Nature 540:371–378
2. Bechthold M, Weaver JC (2017) Materials science and architecture. Nat Rev Mater 2:17082
3. Wen X et al (2021) 3D-printed silica with nanoscale resolution. Nat Mater 20:1506–1511
4. Tumbleston JR et al (2015) Continuous liquid interface production of 3D objects. Science 347:1349–1352
5. Ahn BY et al (2009) Omnidirectional printing of flexible, stretchable, and spanning silver microelectrodes. Science 323:1590–1593

6. Cho H et al (2020) Direct optical patterning of quantum dot light-emitting diodes via in situ ligand exchange. Adv Mater 32:2003805
7. Kim JH et al (2015) 3D Printing of reduced graphene oxide nanowires. Adv Mater 27:157–161
8. Zhang H et al (2021) Biocompatible light guide-assisted wearable devices for enhanced UV light delivery in deep skin. Adv Funct Mater 31:2100576
9. Zhu Z, Ng DWH, Park HS, McAlpine M (2020) C. 3D-printed multifunctional materials enabled by artificial-intelligence-assisted fabrication technologies. Nat Rev Mater 6:27–47
10. Zeng M, Zhang Y (2019) Colloidal nanoparticle inks for printing functional devices: emerging trends and future prospects. J Mater Chem A 7:23301–23336
11. Wang Y, Fedin I, Zhang H, Talapin DV (2017) Direct optical lithography of functional inorganic nanomaterials. Science 357:385–388
12. Liu S-F et al (2022) 3D nanoprinting of semiconductor quantum dots by photoexcitation-induced chemical bonding. Science 377:1112–1116
13. Lee MS, Yee DW, Ye M, Macfarlane RJ (2022) Nanoparticle Assembly as a Materials Development Tool. J Am Chem Soc 144:3330–3346
14. Boles MA, Engel M, Talapin DV (2016) Self-Assembly of Colloidal Nanocrystals: From Intricate Structures to Functional Materials. Chem Rev 116:11220–11289
15. Santos PJ, Gabrys PA, Zornberg LZ, Lee MS, Macfarlane RJ (2021) Macroscopic materials assembled from nanoparticle superlattices. Nature 591:586–591
16. Talapin DV, Lee J-S, Kovalenko MV, Shevchenko EV (2009) Prospects of Colloidal Nanocrystals for Electronic and Optoelectronic Applications. Chem Rev 110:389–458
17. Yao Y et al (2022) High-entropy nanoparticles: Synthesis-structure-property relationships and data-driven discovery. Science 376:eabn3103
18. Lee H-E et al (2018) Amino-acid- and peptide-directed synthesis of chiral plasmonic gold nanoparticles. Nature 556:360–365
19. Gaponik N, Herrmann A-K, Eychmüller A (2011) Colloidal Nanocrystal-Based Gels and Aerogels: Material Aspects and Application Perspectives. J Phys Chem Lett 3:8–17
20. Ziegler C et al (2017) Modern Inorganic Aerogels. Angew Chem Int Ed 56:13200–13221
21. Green AM et al (2022) Assembling Inorganic Nanocrystal Gels. Nano Lett 22:1457–1466
22. Phattharasupakun N, Wutthiprom J, Duangdangchote S, Sawangphruk M (2019) A 3D free-standing lithiophilic silver nanowire aerogel for lithium metal batteries without lithium dendrites and volume expansion: in operando X-ray diffraction. Chem Commun 55:5689–5692
23. Ghaderi S et al (2018) Thermoelectric characterization of nickel-nanowires and nanoparticles embedded in silica aerogels. AIP Adv 8:065221
24. Jiang X, Du R, Hübner R, Hu Y, Eychmüller (2021) A. A roadmap for 3D metal aerogels: materials design and application attempts. Matter 4:54–94

25. Wan W, Zhang R, Ma M, Zhou Y (2018) Monolithic aerogel photocatalysts: a review. J Mater Chem A 6:754–775
26. Cheng W, Rechberger F, Niederberger M (2016) Three-Dimensional Assembly of Yttrium Oxide Nanosheets into Luminescent Aerogel Monoliths with Outstanding Adsorption Properties. ACS Nano 10:2467–2475
27. Pala IR, Brock SL (2012) ZnS Nanoparticle Gels for Remediation of Pb^{2+} and Hg^{2+} Polluted Water. ACS Appl Mater Interfaces 4:2160–2167
28. Burpo FJ et al (2017) Direct solution-based reduction synthesis of Au, Pd, and Pt aerogels. J Mater Res 32:4153–4165
29. Xu X et al (2015) Self-Sensing, Ultralight, and Conductive 3D Graphene/Iron Oxide Aerogel Elastomer Deformable in a Magnetic Field. ACS Nano 9:3969–3977
30. Bag S, Gaudette AF, Bussell ME, Kanatzidis MG (2009) Spongy chalcogels of non-platinum metals act as effective hydrodesulfurization catalysts. Nat Chem 1:217–224
31. Müller A et al (1981) Transition metal thiometalates: properties and significance in complex and bioinorganic chemistry. Angew Chem Int Ed 20:934–955
32. Feng J et al (2021) Printed aerogels: chemistry, processing, and applications. Chem Soc Rev 50:3842–3888
33. Guo F et al (2018) Highly stretchable carbon aerogels. Nat Commun 9:881
34. Zhao S et al (2020) Additive manufacturing of silica aerogels. Nature 584:387–392
35. Wang L et al (2021) Three-dimensional-printed silica aerogels for thermal insulation by directly writing temperature-induced solidifiable inks. ACS Appl Mater Interfaces 13:40964–40975
36. He P et al (2018) Patterned carbon nitride-based hybrid aerogel membranes via 3D printing for broadband solar wastewater remediation. Adv Funct Mater 28:1801121
37. Zhu C et al (2018) Toward digitally controlled catalyst architectures: hierarchical nanoporous gold via 3D printing. Sci Adv 4:eaas9459
38. Liu W et al (2015) Noble metal aerogels-synthesis, characterization, and application as electrocatalysts. ACC Chem Res 48:154–162
39. Long JW et al (2004) Nanocrystalline iron oxide aerogels as mesoporous magnetic architectures. J Am Chem Soc 126:16879–16889
40. Ban HW et al (2016) Molybdenum and tungsten sulfide ligands for versatile functionalization of all-inorganic nanocrystals. J Phys Chem Lett 7:3627–3635
41. Herrmann A-K et al (2013) Multimetallic aerogels by template-free self-assembly of Au, Ag, Pt, and Pd nanoparticles. Chem Mater 26:1074–1083
42. Li Q et al (2019) Review of printed electrodes for flexible devices. Front Mater Sci 5:77
43. Jiang R, Li B, Fang C, Wang J (2014) Metal/semiconductor hybrid nanostructures for plasmon-enhanced applications. Adv Mater 26:5274–5309

Methods

Chemicals

Gold( ) chloride trihydrate ($HAuCl_4 \cdot 3H_2O$, 99.9% trace metal basis, Aldrich), chloroplatinic acid hexahydrate ($H_2PtCl_6 \cdot 6H_2O$, ACS reagent 37.5% Pt basis, Aldrich), iron( ) chloride tetrahydrate ($FeCl_2 \cdot 4H_2O$, puriss. p.a. 99%, Aldrich), silver nitrate ($AgNO_3$, 99% ACS reagent, Aldrich), copper( ) acetylacetonate $(Cu(acac)_2$, 99.9% trace metal basis, Aldrich), platinum( ) acetylacetonate $(Pt(acac)_2$, 97%, Aldrich), iron( ) acetylacetonate $(Fe(acac)_3$, 99.9%, Aldrich), cadmium oxide (CdO, 99.99% trace metal basis, Aldrich), selenium powder (Se, 200 mesh 99.999% metal basis, Alfa Aesar), borane tert-butylamine complex (TBAB, 97%, Aldrich), 1,2,3,4-tetrahydronaphthalene (tetralin, 97%, Alfa Aesar), butylamine (99.5%, Aldrich), palmitic acid (99%, Aldrich), 1,2-hexadecanediol (90%, Aldrich), oleic acid (OA, 90%, Aldrich), oleyl amine (OLAm, 70%, Aldrich), trioctylphosphine (TOP, 90%, Aldrich), 1-octadecene (ODE, 90%, Aldrich), dioctyl ether (99%, Aldrich), phenyl ether (99%, Acros organics), ammonium tetrathiomolybdate (ATTM, 99.97%, Aldrich), nitrosyl tetrafluoroborate ($NOBF_4$, 95%, Aldrich), trichloro(1H,1H,2H,2H-perfluorooctly)silane (PFOCTS, 97%, Aldrich), (3-aminopropyl)triethoxysilane (APTES, 99%, Aldrich), N-methylformamide (NMF, 99%, Aldrich), N,N-dimethylformamide (DMF, 99.8%, Aldrich), hexane (anhydrous 95%, Aldrich), toluene (anhydrous 99.8%, Aldrich), ethyl acetate (EA, 99.5%, SAMCHUN), tetrahydrofuran (THF, 99.5%, SAMCHUN), acetonitrile (anhydrous 99.8%, Sigma), N-methyl-2-pyrrolidone (NMP, anhydrous 99.5%, Sigma), dimethyl sulfoxide (DMSO, 99.9%, Sigma), dichloromethane (DCM, 99.8%, Sigma), chloroform (99.5%, SAMCHUN), pentanol (99%, Sigma), hexanol (98%, Sigma), cyclohexane (99%, Sigma), octane (95%, SAMCHUN), 1-butanol (BtOH, 99%, SAMCHUN), ethanol (99.5%, SAMCHUN), methanol (99.5%, SAMCHUN), 2-propanol (IPA, 99.5%, SAMCHUN), and acetone (99.5%, SAMCHUN). All the chemicals were used as received, without further purification.

Synthesis of colloidal nanocrystal inks

Au nanocrystals. Au nanocrystals were synthesised using a modified method based on a previous report[44]. 6 nm-sized Au seed nanocrystals were synthesised first. $HAuCl_4$ (0.2 g), tetralin (10 mL), and OLAm (10 mL) were mixed into three-neck round bottom flask at room temperature under N_2 flow and vigorous magnetic stirring. TBAB (0.5 mmol), tetralin (1 mL), and OLAm (1 mL) were mixed via sonication for 1 h at room temperature. The solution was then injected into the $HAuCl_4$ solution and stirred for 1 h at room temperature. Acetone was added to the mixture, and centrifuged (7500 rpm, 5 min) to collect 6 nm Au seeds. 8 nm Au nanocrystals were synthesized using the synthesised Au seeds. $HAuCl_4$ (0.1 g) was dissolved in ODE (10 mL) and OLAm (10 mL) at room temperature under N_2 flow in three-neck round bottom flask. 6 nm Au seeds (30 mg) were added to a solution and the reaction solution was heated to 80 °C for 12 min and kept at this temperature for 2 h. Afterward, the heat source was removed, and the product solution was allowed to cool to room temperature. Ethanol was added to the mixture and centrifuged (7500 rpm, 5 min) to remove any unreacted residue. The Au nanocrystals were then dissolved in hexane.

Ag nanocrystals. Ag nanocrystals were synthesised using a modified method based on a previous report[45]. $AgNO_3$ (1.7 g), $Cu(acac)_2$ (0.2 g), and toluene (3.468 mL) were mixed into three-neck round bottom flask at room temperature. Butylamine (1.352 mL) and palmitic acid (0.5 g) were added to this mixed solution. The reaction mixture was heated to 110 °C for 17 min and kept at this temperature for 2 h. Afterward, the heat source was removed, and the product solution was allowed to cool to room temperature. Methanol was added to the mixture, and centrifuged (7500 rpm, 5 min) to remove any unreacted residue. The Ag nanocrystals were then dissolved in hexane.

FePt nanocrystals. FePt nanocrystals were synthesised using a modified method based on a previous report[46]. $Pt(acac)_2$ (0.196 g), $Fe(acac)_3$ (0.177 g), reducing agent 1,2-hexadecanediol (1.292 g), OA (0.16 mL), OLAm (0.164 mL), and dioctyl ether (20 mL) were mixed into three-neck round bottom flask at room temperature in glove box. The reaction mixture was heated to reflux at 286 °C and kept at this temperature for 30 min. Afterward, the heat source was removed, and the product solution was allowed to cool to room temperature. Ethanol was added to the mixture and centrifuged (7500 rpm, 5 min) to remove any unreacted residue. The FePt nanocrystals were then dissolved in hexane.

CdSe nanocrystals. CdSe nanocrystals were synthesised using a modified method based on a previous report[47]. CdO (0.255 g), OA (3.11 mL), and ODE (35 mL) were mixed into three-neck round bottom flask at room temperature in glove box. The solution was heated to 180 °C for 31 min and kept at this temperature for 1 h to form a clear solution under N_2 atmosphere. Subsequently, the solution was heated up to 250 °C for 14 min. TOP-Se solution of Se (0.051 g), TOP (0.3 mL), and ODE (5 mL) were mixed and stirred more than 1 h in glove box. The TOP-Se solution was then injected into the CdO solution and stirred for 2 min. Afterward, the heat source was removed, and the product solution was allowed to cool to room temperature. Methanol, acetone, IPA were added to the mixture and centrifuged (7500 rpm, 5 min) to remove any unreacted residue. The CdSe nanocrystals were then dissolved in hexane.

Fe_3O_4 nanocrystals. Fe_3O_4 nanocrystals were synthesised using a modified method based on a previous report[48]. $Fe(acac)_3$ (0.7063 g), 1,2-hexadecanediol (2.5844 g), OA (1.91 mL), OLAm (1.975 mL), and phenyl ether (20 mL) were mixed into three-neck round bottom flask at room temperature in glove box. The reaction mixture was heated to 200 °C for 35 min under flow of N_2, and then kept at this temperature for 30 min. Subsequently, the mixture was heated to 265 °C for 13 min, then kept at this temperature for 30 min. The black-brown mixture was cooled to room temperature by removing the heat source. Ethanol was added to the mixture, and centrifuged (6000 rpm, 5 min) to remove any unreacted residue. The Fe_3O_4 nanocrystals were dissolved in hexane.

Synthesis of inorganic ligands-capped nanocrystal inks. Negative charges on the surfaces of nanocrystals were introduced by the ligand exchange process. All ligand exchange reactions were performed in a N_2-filled glovebox using a typical two-phase ligand-exchange strategy[49]. ATTM was exploited as an inorganic ligand to replace the existing organic ligands. ATTM (0.9 g) was dissolved in NMF (30 mL) and stirred for 10 min. Then, 10 mL of nanocrystals containing hexane solution (30 mg mL^-

^{1}) was added to a vial containing 30 mL of ATTM solution (30 mg mL^{-1}). The mixture was vigorously stirred until the phase transfer of nanocrystals from the upper hexane phase to the bottom NMF phase was completed. After ligand exchange, the upper hexane phase was discarded, and the bottom layer of ATTM-capped nanocrystals was collected by the addition of IPA (210 mL). The purification step was repeated two times to collect the ATTM-capped nanocrystals.

For the case of Fe_3O_4 nanocrystals, the two-phase ligand exchange process cannot be adopted directly. The ligand stripping process was conducted first to remove the existing organic ligands[50]. $NOBF_4$ (0.9 g) was dissolved in DMF (30 mL) and stirred for 10 min. To form an immiscible two-phase mixture, 10 mL of nanocrystals in hexane (30 mg mL^{-1}) was added to a vial containing 30 mL of $NOBF_4$ solution (30 mg mL^{-1}). The immiscible two-phase mixture was vigorously stirred until the phase transfer of nanocrystals from the upper hexane phase to the bottom $NOBF_4$ phase is completed. After ligand stripping, the upper hexane phase was discarded, and the bottom solution was collected by the addition of toluene (210 mL). The purification step was repeated two times to remove unreacted $NOBF_4$ species. The stripped nanocrystals were redispersed in 30 mL of ATTM stock solution (30 mg mL^{-1}) and stirred overnight. The solution was precipitated by the addition of IPA (210 mL) to collect the ATTM-capped Fe_3O_4 nanocrystals.

The ATTM- capped nanocrystals were dispersed in NMF to form stable colloidal solution with concentration of 25 mg mL^{-1} (Ag), 50 mg mL^{-1} (Au), 45 mg mL^{-1} (FePt), 50 mg mL^{-1} (CdSe), and 70 mg mL^{-1} (Fe_3O_4). A colloidal solution of ATTM-capped nanocrystals was exploited as 3D printing ink without any organic additives.

Hansen solubility parameter(HSP) difference (R_a) calculations

The HSPs indicate the cohesive energy density of a chemical resulting from the interactions of a given solvent molecule[51]. The energy needed to break all the cohesive bonds involves dispersion force, permanent dipole-permanent dipole forces, and hydrogen bonding. Thus, the total solubility parameter can be calculated in eq 1

$$\delta_t^2 = \delta_d^2 + \delta_p^2 + \delta_h^2 \quad (1)$$

Where δ_t ($MPa^{1/2}$) is the solubility parameter and δ_d, δ_p, and δ_h are the dispersion force, dipole interaction force, and hydrogen bonding force term, respectively. R_a is the difference between the HSPs of two materials, given by eq 2

$$R_a^2 = \{4(\delta_{d1} - \delta_{d2})^2 + (\delta_{p1} - \delta_{p2})^2 + (\delta_{h1} - \delta_{h2})^2\} \quad (2)$$

A smaller R_a indicates that the HSP of the two materials are likely to be miscible.

Dielectric constants of solvents were obtained in the ref. 52.

Wet 3D microprinting process of inorganic nanocrystals

Preparation of micronozzles, substrates, and linker containing solidification baths. The borosilicate glass capillaries were cleaned by rinsing with methanol, acetone, and IPA under sonication for 5 min each. The borosilicate glass capillaries were pulled to prepare a nozzle with a pipette puller (P-1000, Sutter Instruments). The pipette-pulling parameters, such as heat, pull, velocity, time, delay, and pressure, were tuned to fabricate diameter- and morphology-controlled glass pipettes. The pre-pulled glass pipettes were O_2-plasma treated for surface hydrophilisation. Hydrophobic surface treatment was performed by a PFOCTS self-assembled monolayer (SAM) deposition step using a vapour-phase technique. The trichlorosilane-based head groups reacted with the hydroxyl group on the substrate to form a stable covalent bond. The PFOCTS SAM-coated glass pipettes were thermally treated at 120 °C for 20 min and rinsed with hexane to remove the unreacted PFOCTS species. The Si wafers were cleaned by rinsing with methanol, acetone, and IPA under sonication for 5 min each. The clean Si substrates were O_2-plasma treated for surface hydrophilisation. Hydrophilic surface treatment was performed via APTES SAM deposition using a vapour-phase technique. The triethoxysilane-based head groups reacted with the hydroxyl group on the substrate to form a stable covalent bond. The APTES SAM-coated substrates were thermally treated at 100 °C for 30 min and rinsed with toluene to remove the unreacted APTES species. Finally, the linker baths were prepared by dissolving $HAuCl_4$, H_2PtCl_6, and $FeCl_2{\cdot}4H_2O$ in 1-butanol to obtain 0.5–1 mM solution.

Wet 3D microprinting procedure. The printing machine consisted of a micronozzle connected to a dispenser (Ultimus 2, Nordson EFD) and a three-axis (*x*,*y*,*z*) stepping motor nanostage (Aerotech). The inorganic ligand-capped nanocrystals were loaded into a PFOCTS SAM-coated micronozzle, and the inks were pneumatically driven through a micronozzle at 2.1–100 kPa. The APTES SAM-coated Si substrate was attached to a glass petri dish and placed on a three-axis (*x*,*y*,*z*) nanostage. The distance between the micronozzle and the substrate was fixed at 10 μm. After controlling the distance, the linker bath solution was poured into a glass petri dish. Their positions and moving speeds were accurately controlled in real time using a motion composer software (A3200, Aerotech). The stage was translated at a speed of 1.2 mm s^{-1} during printing and the overall process was monitored using a side-view charge coupled device (CCD) camera (MicroPublisher 5.0 RTV, QImaging). Also, the videos showing the printing process were recorded using a CCD camera (Supplementary Video 1-3).

Supercritical drying. The printed object was solvent-exchanged with fresh butanol at 25 °C several times. After a complete exchange of the solvent, the printed wet state objects were transferred into a supercritical fluid extractor (SFT-110XW, Supercritical Fluid Technologies Inc.) with an excess amount of butanol to prevent the evaporation of the solvents. The chamber was flushed with liquid CO_2 to exchange the butanol. To convert the liquid CO_2 to the supercritical state, the vessel was pressurised and heated to 1800 psi and 60 °C, respectively. The butanol-CO_2 mixture was extracted continuously through the exit of the vessel until all solvents were removed.

Characterisations

Microscopy analyses. The dimension and microstructure of the printed inorganic nanocrystal-based porous materials were imaged using OM and SEM, respectively. Optical imaging was performed using an OM (BX51M, Olympus). SEM (including tilted views) and EDS mapping image were collected using a field-effect SEM (Nova NanoSEM, FEI and SU7000, Hitachi High-Tech) with a 10 kV (SEM image) and 20 kV (EDS mapping image) electron beam. The CCD images and videos were obtained using a CCD camera (MicroPublisher 5.0 RTV, QImaging). The TEM images were obtained at 200 kV using a JEOL-2100 microscope (JEOL). HR-TEM, HAADF-STEM imaging, and spectral imaging based on STEM-EDS were performed at 200 kV using a JEM-2100F microscope (JEOL). For analysis, the printed objects were crushed and suspended in methanol by ultrasound for 15–120 s, depending on their dispersing ability.

N_2 adsorption/desorption analysis. The sample porosities were determined using an N_2 sorption analyser (BELSORP-Max, BEL) operated at 77 K. Prior to the measurements, the sample surfaces were evacuated at 70 °C for 12 h under vacuum conditions to clean the surfaces. The specific surface areas of the samples were calculated using the BET equation, while their pore size distributions were derived from the adsorption branches of the isotherms using the BJH (Barrett-Joyner-Halenda) method. The silica equivalent surface areas were calculated by the relative density method[53]. Here, the density of silica is assumed to be an average density of quartz (2.65 mg cm^{-3}), tridymite (2.31 mg cm^{-3}), and cristobalite (2.33 mg cm^{-3}), 2.43 mg cm^{-3}.

X-ray diffraction analysis. The XRD patterns were obtained using a high-power X-ray diffractometer (D/MAX2500V/PC, Rigaku) equipped with Cu Kα radiation and operated at 40 kV and 200 mA.

ζ-potential analysis. The ζ-potential data were collected using a Zetasizer Nano ZS instrument (Malvern). Inorganic ligand-capped Ag nanocrystals were measured before and after exposure to Au^{3+}, Pt^{4+}, and Fe^{2+} linker solution, respectively.

X-ray photoelectron spectroscopy. XPS spectra were acquired using an X-ray photoelectron spectrometer (ESCALAB 250XI, Thermo Fisher Scientific) with a monochromatic Al Kα X-ray source (1,486.6 eV). All XPS spectra were corrected with adventitious C 1s peak at 284.8 eV. For analysis, inorganic ligand-capped Ag nanocrystals were printed on the Si substrate filled with butanol, Au^{3+}, Pt^{4+}, and Fe^{2+} linker

solutions, respectively. After drying with a supercritical fluid, all the samples were kept in a glove box to prevent oxidation before analysis.

Thermal stability analysis. The thermal stability of the printed Au nanocrystal-based porous material was investigated by thermogravimetric analysis (TGA Q500, TA Instruments) in the temperature range of 25–700 °C at a heating rate of 10 °C min^{-1} under a nitrogen atmosphere.

Magnetic property measurement. The magnetic property was measured by using a superconducting quantum interference device-vibrating sample magnetometer (SQUID-VSM, Quantum Design).

Optical property measurement. The UV-vis absorption spectra were measured using a UV-vis spectrophotometer (UV-2600, Shimadzu). The photoluminescence spectra were investigated using a UV-Vis-NIR spectrophotometer (Cary 5000) at room temperature. For analysis, wet state CdSe was prepared by extruding inorganic ligand-capped CdSe nanocrystals (1 mL) into the 0.5 mM concentration of Fe^{2+} linker solution (50 mL). The subsequent supercritical drying process can produce the dried state CdSe powder. The obtained dried state CdSe was suspended in NMF by ultrasound for 120 s. To investigate the specific oxidation effect on the optical properties, CdSe wet state and dried state dispersions were treated under UV irradiation under the air atmosphere for 24 h.

Electrical property measurement. The electrical conductivity was measured by a four-point van der Pauw method (Keithley 2,400 multimeter controlled by Lab trace 2.0 software, Keithley Instrument, Inc.). For analysis, inorganic ligand-capped Au nanocrystal inks (5 µl) were casted on the Si substrate filled with 0.5 mM Au^{3+} linker solution (2 mL) followed by supercritical drying process to produce the Au aerogel film. For the preparation of xerogel films, the solvent was evaporated in ambient conditions. After complete evaporation of the solvent, a homogeneous film was formed on the substrate. The Au xerogel film was heat treated at 600 °C for 1 h with a ramping rate of 5 °C min^{-1} under H_2 (99.999%) in a tube furnace.

Data availability

The data that support the plots within this paper and other findings of this study are available from the corresponding author upon reasonable request.

44 Zhu, W. *et al.* Monodisperse Au nanoparticles for selective electrocatalytic reduction of CO_2 to CO. *J. Am. Chem. Soc.* **135**, 16833-16836 (2013).

45 Jun, B.-H., Lee, K.-J., Cho, H.-J. & Joung, J.-W. Method for producing silver nanoparticles and conductive ink. US20090223410A1 (2009).

46 Liu, C. *et al.* Reduction of sintering during annealing of FePt nanoparticles coated with iron oxide. *Chem. Mater.* **17**, 620-625 (2005).

47 Chen, J. *et al.* An oleic acid-capped CdSe quantum-dot sensitized solar cell. *Appl. Phys. Lett.* **94**, 153115 (2009).

48 Sun, S. & Zeng, H. Size-controlled synthesis of magnetite nanoparticles. *J. Am. Chem. Soc.* **124**, 8204-8205 (2002).

49 Kovalenko, M. V., Scheele, M. & Talapin, D. V. Colloidal nanocrystals with molecular metal chalcogenide surface ligands. *Science* **324**, 1417-1420 (2009).

50 Gu, D. H. *et al.* Colloidal suprastructures self-organised from oppositely-charged all-inorganic nanoparticles. *Chem. Mater.* **32**, 8662-8671 (2020).

51 Hansen, C. M. *Hansen Solubility Parameters A User's Handbook. Journal of Chemical Information and Modeling,* 2nd Ed., CRC Press, Boca Raton (2007).

52 Maryott, A. A. & Smith, E. R. *Table of Dielectric Constants of Pure Liquids*, National Bureau of Standards, Washington D. C. (1951).

53 Yu, H. & Brock, S. L. Effects of nanoparticle shape on the morphology and properties of porous CdSe assemblies (aerogels). *ACS Nano* **2**, 1563-1570 (2008).

Declarations

Acknowledgments

We acknowledge the Nano·Material Technology Development Program (NRF-2018M3A7B8060697), the mid-career researcher program (NRF-2022R1A2C3009129 and NRF-2021R1A2C2007495), and the Creative Materials Discovery Program (NRF-2020M3D1A1110502) through the National Research Foundation of the Republic of Korea (NRF) funded by Ministry of Science and ICT, and the UNIST Research Fund (1.220024.01).

Author contributions

M.S. and J.S.S. designed the experiments, analysed the data, and wrote the paper. M.S., Y.K., B.V.C., S.E.Y., D.H.G., R.S.R. carried out the synthesis and basic characterisation of materials. M.S., D.S.B., and S.H.J. performed the characterisation of porosity. S.L. and J.-W.Y. performed the characterisation of magnetic properties. All authors discussed the results and edited and commented on the manuscript.

Competing interests

Ulsan National Institute of Science and Technology (UNIST) has filed a patent, PCT/KR2022/003817 (inventors: M.S., Y.K., and J.S.S.) that covers the wet 3D microprinting chemistry and methods reported in this article.

Figures

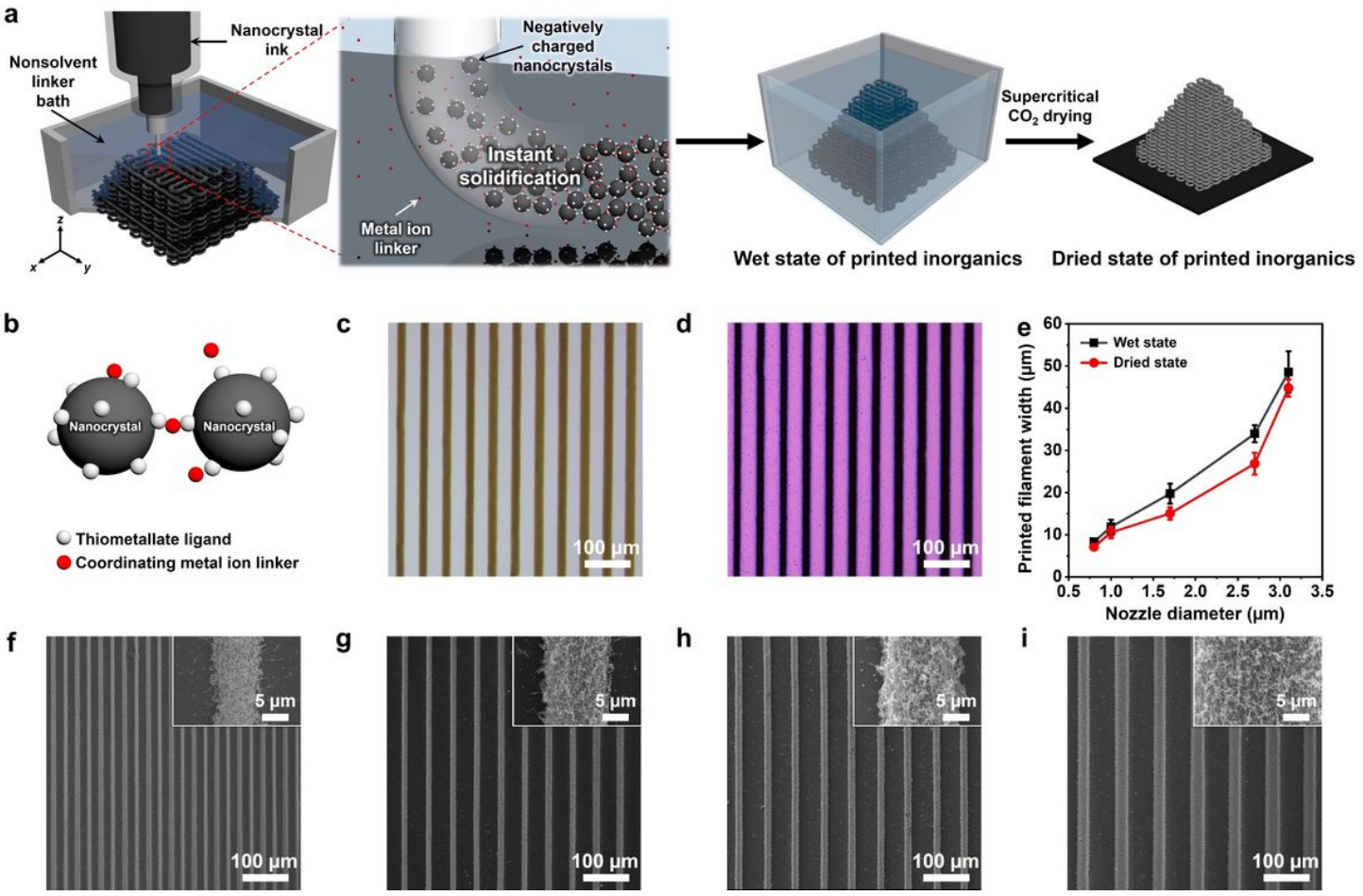

Figure 1

3D microprinting of inorganic nanocrystals. a, Scheme for wet 3D microprinting of inorganic nanocrystal-based porous materials. **b,** Schematic illustration of linking of all-inorganic nanocrystals with coordinating metal ions. The components are colour-coded as follows: grey, nanocrystal; white, thiometallate anion ligand; red, metal ion linker. **c,d,** OM images in wet state (**c**) and dried state (**d**) of printed multilayer Ag filaments. **e,** Widths of printed Ag filaments as a function of nozzle diameter for the wet state and dried state. **f–i,** SEM images of multilayer Ag filaments patterned with feature widths of 7- (**f**), 11- (**g**), 15- (**h**), and 27-μm (**i**). Insets: high magnification SEM images of corresponding filaments.

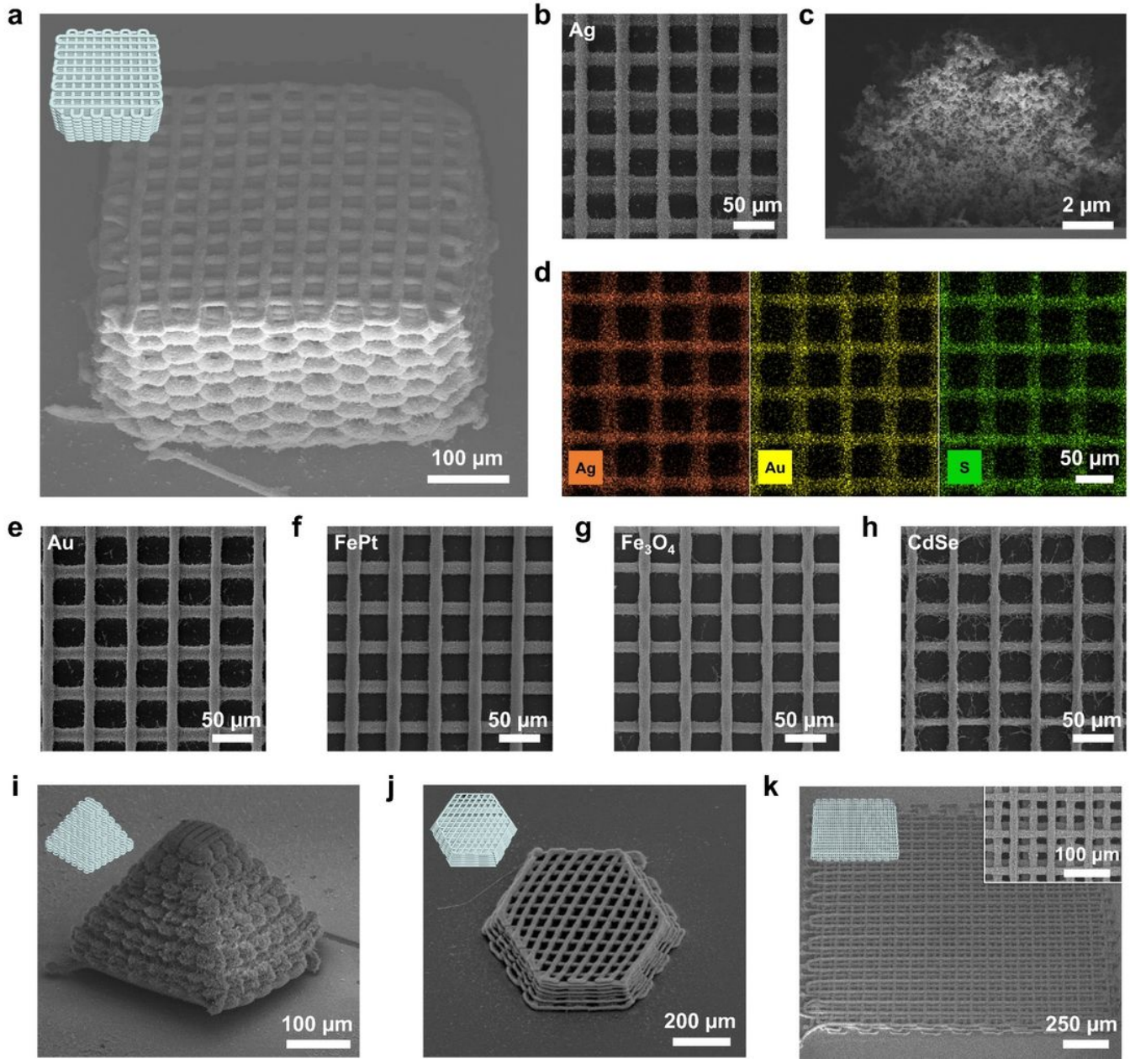

Figure 2

Printed 3D microarchitectures of inorganic porous materials. a, 32-layer lattice cube illustration model (inset) and SEM image of 3D-printed Ag. **b,** Top view of SEM image of 3D-printed Ag lattice cube. **c,** Cross-sectional SEM image of printed Ag filament. **d,** EDS mapping image of printed Ag comprising Ag nanocrystals (orange), Au-based linkers (yellow) and S-based ligands (green). **e–h,** SEM images of 3D lattice structures of Au (**e**), FePt (**f**), Fe_3O_4 (**g**), and CdSe (**h**). **i,** 36-layer pyramid illustration model (inset) and SEM image of 3D-printed CdSe. **j,** 12-layer hexagonal prism illustration model (inset) and SEM image of 3D-printed FePt. **k,** 8-layer large-scale square lattice structure illustration (left inset) and SEM image of 3D-printed Ag. Right inset: magnified SEM image of printed structure.

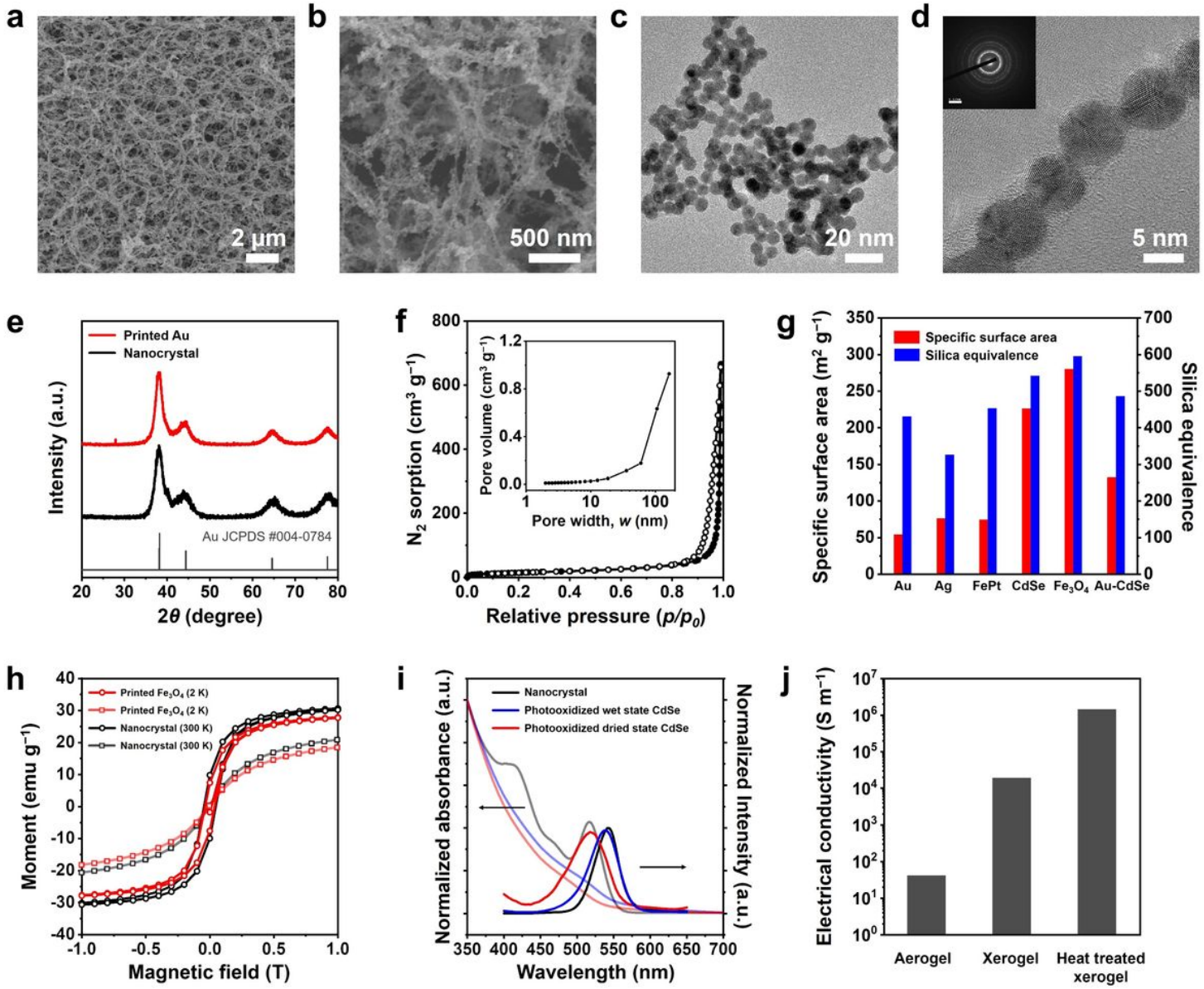

Figure 3

Microstructural characteristics and functionalities of the 3D-printed materials. a,b, HRSEM images of printed Au nanocrystals. **c,d,** TEM (**c**) and HRTEM (**d**) images of printed Au nanocrystals. Inset in the panel (d): electron diffraction pattern. **e,** XRD patterns of as-synthesised Au and printed Au nanocrystals. **f,** N_2 physisorption isotherms of printed Au sample at 77 K. Inset: pore size distribution derived from Barrett-Joyner-Halenda (BJH) analysis. **g,** Summarised specific surface areas and silica equivalents of printed inorganic porous materials. **h,** Magnetic hysteresis loops of as-synthesised Fe_3O_4 (black) and printed nanocrystals (red) measured at 2 K and 300 K. **i,** UV-Vis absorption and PL spectrum of CdSe nanocrystals (black) and printed wet (blue), and dried (red) samples. **j,** Electrical conductivities of printed Au porous sample, xerogel, and sintered sample.

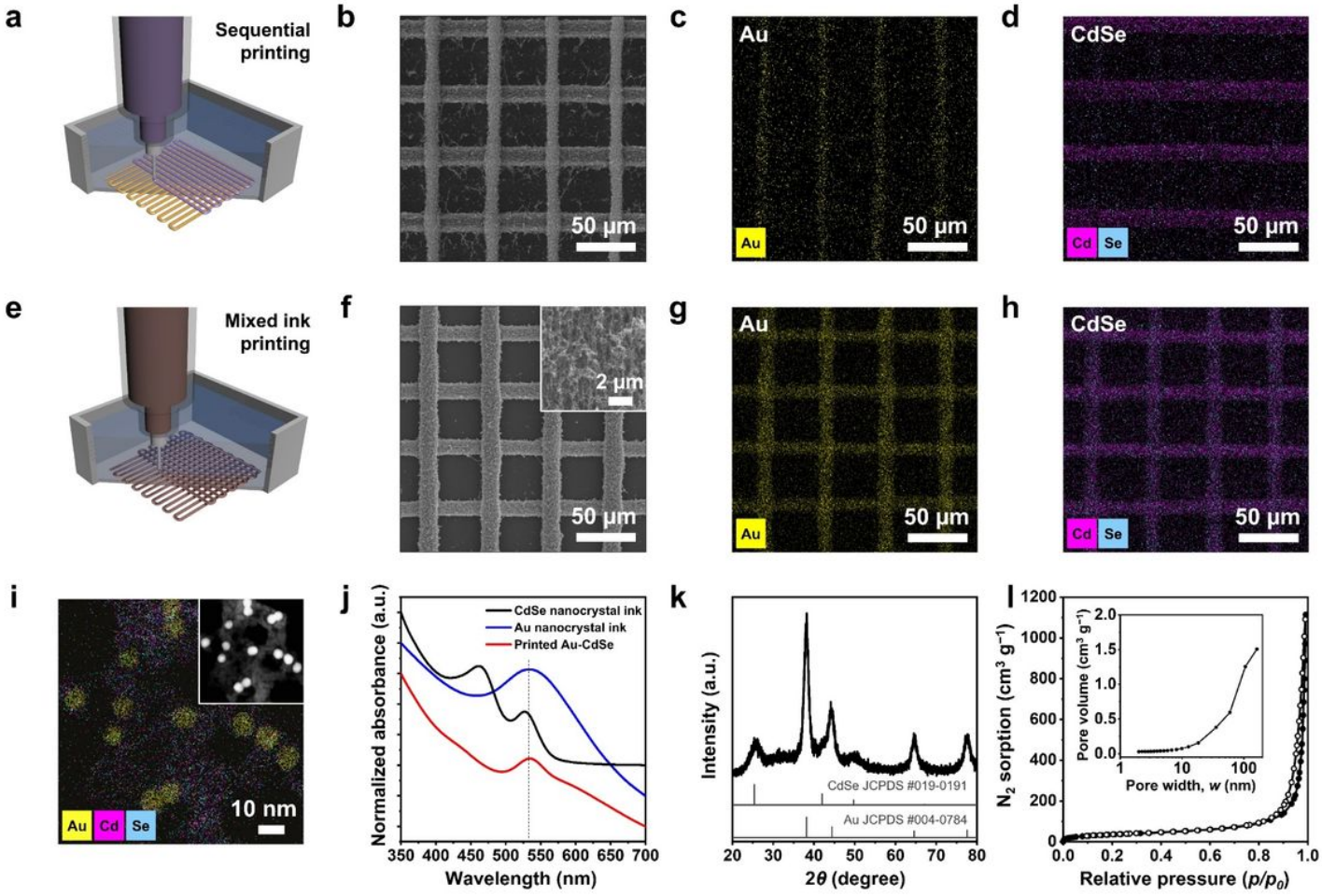

Figure 4

3D printing of multi-material nanocrystals. a, Scheme for sequential deposition of multiple nanocrystal inks for CdSe and Au nanocrystals. **b,** SEM image of sequentially printed Au (vertical) and CdSe (horizontal). **c,d,** EDS mapping image of Au (yellow) (**c**) and Cd (purple) (**d**). **e,** Scheme for 3D printing of mixed inks containing CdSe and Au nanocrystals. **f,** SEM image of printed Au-CdSe composite. Inset: HRSEM image of printed Au-CdSe. **g,h,** EDS analysis of Au (yellow) (**g**) and Cd (purple) (**h**). **i**, Phase analysis of mixed Au-CdSe nanocrystals using HAADF-STEM (inset) and STEM-EDS mapping of Au (yellow), Cd (purple), and Se (blue). **j,** UV-Vis absorption spectra of thiomolybdate-capped CdSe (black) and Au (blue) nanocrystal ink, and printed Au-CdSe composite (red). **k,** XRD pattern of printed Au-CdSe nanocrystals. The vertical lines indicate the bulk references of CdSe and Au. **i,** N_2 physisorption isotherm of printed Au-CdSe nanocrystals. Inset: pore size distribution derived from BJH analysis.

Supplementary Files

This is a list of supplementary files associated with this preprint. Click to download.

- SupplementaryInformation.pdf
- SupplementaryVideo1.mov
- SupplementaryVideo2.mov
- SupplementaryVideo3.mov